

OmniGS: Omnidirectional Gaussian Splatting for Fast Radiance Field Reconstruction using Omnidirectional Images

Longwei Li, Huajian Huang, Sai-Kit Yeung and Hui Cheng*

Abstract—Photorealistic reconstruction relying on 3D Gaussian Splatting has shown promising potential in robotics. However, the current 3D Gaussian Splatting system only supports radiance field reconstruction using undistorted perspective images. In this paper, we present OmniGS, a novel omnidirectional Gaussian splatting system, to take advantage of omnidirectional images for fast radiance field reconstruction. Specifically, we conduct a theoretical analysis of spherical camera model derivatives in 3D Gaussian Splatting. According to the derivatives, we then implement a new GPU-accelerated omnidirectional rasterizer that directly splats 3D Gaussians onto the equirectangular screen space for omnidirectional image rendering. As a result, we realize differentiable optimization of the radiance field without the requirement of cube-map rectification or tangent-plane approximation. Extensive experiments conducted in egocentric and roaming scenarios demonstrate that our method achieves state-of-the-art reconstruction quality and high rendering speed using omnidirectional images. To benefit the research community, the code will be made publicly available once the paper is published.

Index Terms—Omnidirectional Vision, Photorealistic Mapping, 3D Reconstruction, View Synthesis, Gaussian Splatting

I. INTRODUCTION

Reconstructing the three-dimensional (3D) structures of observed environments plays an important role in many robotic applications, such as localization, navigation, path planning, and other high-level perception tasks. Recent progress [1] in this realm has sought to harness the information contained in large field-of-view (FoV) images, especially omnidirectional images for performance enhancement. Owing to a 360-degree field of view (FoV), the omnidirectional cameras are able to capture the entire environment at each shot, providing consistent observations. Therefore, some SLAM systems such as 360VO [2], 360VIO [3], and LF-VISLAM [4] make use of consistent observations to achieve robust pose estimation and efficient reconstruction. However, the conventional use of point clouds and meshes to model reconstructed environments, although effective in capturing structural information, often fails to provide visually appealing representations.

In order to achieve photorealistic reconstruction and enable immersive scene roaming using omnidirectional images, several approaches, such as 360Roam [5], 360FusionNerf [6],

Longwei Li and Hui Cheng* are with the School of Computer Science and Engineering, Sun Yat-Sen University. Email: lilw23@mail2.sysu.edu.cn

Huajian Huang and Sai-Kit Yeung are with the Department of Computer Science and Engineering, The Hong Kong University of Science and Technology. Email: hhuangbg@connect.ust.hk, saikit@ust.hk

*Corresponding author, Email: chengh9@mail.sysu.edu.cn

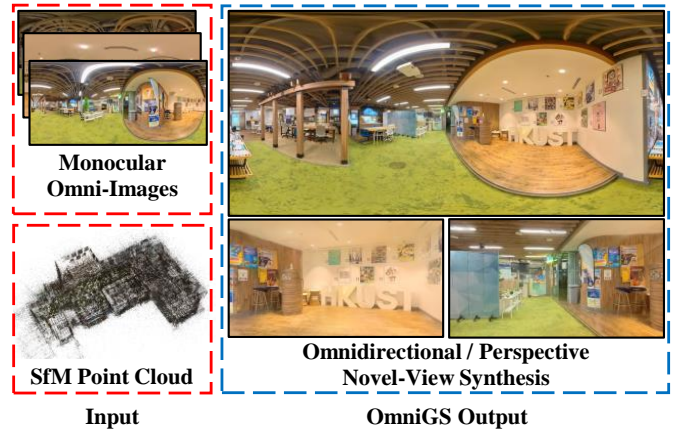


Fig. 1. OmniGS is a novel omnidirectional reconstruction method. It takes a series of calibrated monocular 360 images and their sparse SfM point cloud as input, and reconstructs the scene using 3D Gaussians as representations, achieving real-time novel-view synthesis.

and PaniGRF [7] have explored the utilization of the neural radiance field (NeRF) technique [8]. Unlike traditional methods that focus on precise geometry reconstruction, NeRF employs multi-layer perceptrons (MLPs) to implicitly model the scene. It then accumulates density and view-dependent color per ray, which are regressed from the MLPs, for image synthesis. Meanwhile, the MLP parameters are optimized by minimizing the photorealistic loss between rendered images and corresponding training images. Since such a rendering and optimization process requires millions of ray samplings, NeRF-based methods [5]–[7] suffer from long training or inference time to model omnidirectional radiance field.

In this paper, we propose a novel system called OmniGS, which utilizes omnidirectional Gaussian Splatting for fast radiance field reconstruction. Recently, 3D Gaussian Splatting (3DGS) [9] effectively addresses the limitation of NeRF by introducing 3D Gaussians to explicitly represent radiance field representation. Each 3D Gaussian is a point associated with certain attributes, i.e. position, color, scale, rotation, and opacity. For rendering, the EWA splatting algorithm [10] is applied to project and rasterize 3D Gaussians onto the screen space. Benefiting from the highly efficient rendering process, 3DGS significantly reduces training and inference time in high-quality radiance field reconstruction, having great potential in real-time applications [11]–[14].

Nevertheless, the current splatting algorithm is only compat-

ible with undistorted perspective image rendering. Therefore, we begin by conducting a theoretical analysis of the derivatives of the spherical camera model in 3D Gaussian splatting, which provides the mathematical foundation required for accurate representation and rendering of omnidirectional images. Building upon the derived derivatives, we develop a new GPU-accelerated omnidirectional rasterizer that directly splats 3D Gaussians onto the equirectangular screen space. This approach enables efficient and differentiable optimization of the radiance field without the need for cube-map rectification or tangent-plane approximation. To verify the efficacy of our proposed system, we conducted extensive evaluations on the omnidirectional roaming scenes of 360Roam [5] and egocentric scenes of EgoNeRF [15]. Qualitative and quantitative results show that our method achieves state-of-the-art (SOTA) performance regarding photorealistic reconstruction quality and rendering speed using omnidirectional images.

In summary, our contributions are as follows:

- We introduce thoughtful theoretical analysis of the omnidirectional Gaussian Splatting, enabling direct splatting of the 3D Gaussians onto the equirectangular screen space for real-time and differentiable rendering.
- We develop OmniGS, a novel photorealistic reconstruction system based on our new GPU-accelerated omnidirectional rasterizer, achieving fast and high-fidelity reconstruction.
- The code of OmniGS will be publicly available.

II. RELATED WORKS

A. Large-FoV Sparse Reconstruction

Reconstructing 3D structures of observed environments is a fundamental task that often relies on multi-view geometry and factor graph solvers. Recent advancements have focused on leveraging the information embedded in large field-of-view (FoV) images for efficient and robust reconstruction. Existing methods such as OpenMVG [16] utilize feature points on spherical images to establish 2D-to-3D correspondences and optimize the 3D structure by minimizing spherical re-projection errors. Additionally, techniques such as 360VIO [3] and LF-VISLAM [4] integrate inertial measurement units (IMUs) into the visual system, leading to improved accuracy and robustness in estimating motion structures. In contrast, 360VO [2] pioneers direct visual odometry using a monocular omnidirectional camera, producing semi-dense reconstructed point cloud maps. However, these methods often yield sparse maps that fall short in realistic exploration scenarios.

B. Large-FoV Photorealistic Reconstruction with NeRF

With the advancements in neural radiance field (NeRF) techniques, photorealistic reconstruction has gained increased flexibility. 360Roam [5] first introduced the use of omnidirectional radiance fields for immersive scene exploration. To improve NeRF performance in large-scale scenes, 360Roam utilizes multiple 360-degree images to progressively reconstruct explicit geometry. It further incorporates geometry-aware sampling and decomposition of the global radiance field,

resulting in fast and high-fidelity synthesis of novel views. 360FusionNeRF [6] and PERF [17] aim to reconstruct the radiance field from a single omnidirectional image, alleviating the need for a large training dataset. However, due to the limited information provided by the single image, additional depth maps are necessary to enhance the performance of novel view synthesis, particularly in complex scenes. To address the issue of training view overfitting in NeRF, PanoGRF [7] integrates deep features and 360-degree scene priors into the omnidirectional radiance field. Contrasting the roaming scenarios explored by previous methods, EgoNeRF [15] focuses on egocentric scenes captured within a small circular area using casually acquired omnidirectional images. EgoNeRF employs quasi-uniform angular grids to adaptively model unbounded scenes, achieving state-of-the-art performance in egocentric view synthesis. Despite the success of NeRF-based methods in novel view synthesis using omnidirectional images, the computational intensity of radiance field sampling remains a challenge, leading to slow training or inference speeds.

C. Photorealistic Reconstruction with 3D Gaussian Splatting

Recently, the emergence of 3DGS [12] has opened up new possibilities for real-time applications. Building upon this foundation, GS-SLAM [12] and Splatam [11] utilize 3D Gaussians as a scene representation to perform dense RGB-D SLAM. Similarly, Gaussian Splatting SLAM [18] adopts direct optimization against 3D Gaussians for camera tracking. In addition, Photo-SLAM [14] achieves top photorealistic mapping quality without relying on dense depth optimization. Notably, it can execute online mapping seamlessly on an embedding device at a real-time speed, highlighting its potential for robotics applications.

To extend Gaussian Splatting for omnidirectional image rendering, a concurrent work 360-GS [19] leverages a tangent-plane approximation to formulate the Gaussian splatting process. However, even though 360-GS outperforms previous NeRF-based baselines in terms of omnidirectional image rendering quality and training speed, its two-stage-projection splatting method is suboptimal. Furthermore, its reliance on indoor layout priors limits its generalization capabilities in multi-room scale and outdoor scenarios. In this paper, our proposed OmniGS uses direct screen-space splatting to accelerate rendering and does not rely on scene assumptions or deep networks, enabling its application in diverse indoor and outdoor scenes.

III. OMNIDIRECTIONAL GAUSSIAN SPLATTING

In this section, we will introduce our omnidirectional Gaussian Splatting method, including the omnidirectional camera model, the forward rendering process, and the corresponding backward gradient propagation.

A. Camera Model

The camera model is the mathematical relationship between a 3D camera-space point $\mathbf{t} = [t_x, t_y, t_z]^T$ and its projected position $\mathbf{p} = [p_x, p_y]^T$ on the image. To take advantage of

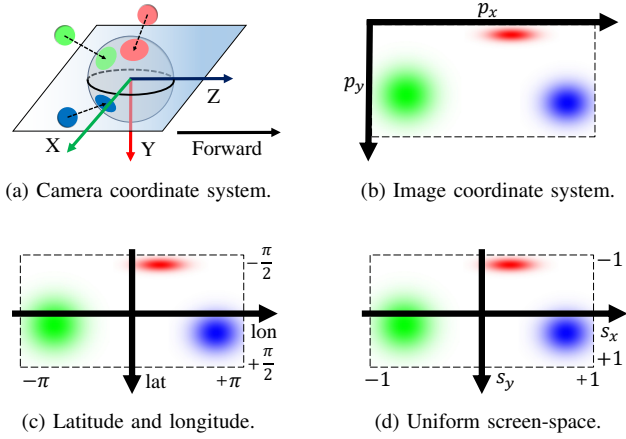


Fig. 2. Coordinate systems used in OmniGS. We use the SLAM convention for cameras, i.e. +X is right, +Y is down, +Z is forward. In the forward rendering process, 3D Gaussians are first transformed from the world coordinate system to the camera space, then projected onto the image. The latitude-longitude coordinate system and the uniform screen-space coordinate system serve as intermediate variables during the projection process. The X-Z plane of the camera space is the equatorial plane, i.e. $lat = 0$.

one-shot omnidirectional images, we use the equirectangular projection model, which is the most commonly used form in the context of omnidirectional reconstruction. As shown in Fig. 2a, we define the camera coordinate system according to the SLAM convention. The camera X-Z plane corresponds to the equatorial plane of equirectangular projection. To keep high fidelity, we use the original inverse trigonometric functions to compute the spherical latitude lat and longitude lon :

$$\begin{bmatrix} lon \\ lat \end{bmatrix} = \begin{bmatrix} \arctan2(t_x/t_z) \\ \arcsin(t_y/t_r) \end{bmatrix}, \quad (1)$$

where $t_r = \sqrt{t_x^2 + t_y^2 + t_z^2}$ is the distance from the center of unit sphere to the center of the 3D Gaussian in the camera space, $\arctan2$ is the 4-quadrant inverse tangent, and we have $-\pi \leq lon < \pi$ and $-\pi/2 \leq lat < \pi/2$. Then the above latitude and longitude (Fig. 2c) can be transformed into the uniform screen-space coordinates (Fig. 2d):

$$\begin{bmatrix} s_x \\ s_y \end{bmatrix} = \begin{bmatrix} lon/\pi \\ 2lat/\pi \end{bmatrix}, \quad (2)$$

so that we have $-1 \leq s_x, s_y < 1$. At the end of the projection process, the uniform screen-space coordinates are transformed into the pixel position on the image (Fig. 2b):

$$\begin{bmatrix} p_x \\ p_y \end{bmatrix} = \begin{bmatrix} (s_x + 1)W/2 \\ (s_y + 1)H/2 \end{bmatrix}, \quad (3)$$

where W, H is the width and height of the equirectangular image respectively, measured in the count of pixels.

B. Forward Rendering

Following 3DGS [9], the final color of each image pixel is decided following the α -blending model:

$$C = \sum_{i=1}^N c_i \alpha_i \prod_{j=1}^{i-1} (1 - \alpha_j), \quad (4)$$

where N is the number of 3D Gaussians near this pixel. For perspective cameras, these Gaussians are sorted by their t_z , from nearest to farthest. However, under the circumstances of omnidirectional vision, the criterion for sorting is changed to t_r . The i -th Gaussian has color c_i and sampled intensity α_i . Furthermore, α_i is determined by its opacity o_i and the sampled value on its 2D Gaussian distribution:

$$\alpha_i = o_i G_i(\Delta \mathbf{p}_i), \quad (5)$$

where $\Delta \mathbf{p}_i = \mathbf{p}_i - \mathbf{p}_s$ is the difference vector between its projected center \mathbf{p}_i and the sampling pixel position \mathbf{p}_s , and the sampling on the 2D Gaussian function is defined as:

$$G_i(\Delta \mathbf{p}_i) = \exp\left(-\frac{1}{2}(\Delta \mathbf{p}_i)^T \tilde{\Sigma}_i^{-1}(\Delta \mathbf{p}_i)\right). \quad (6)$$

To get the 2D covariance $\tilde{\Sigma}$ of the Gaussian projected onto the equirectangular image plane, we compute it according to the local affine approximation method described in [10]:

$$\tilde{\Sigma} \approx \mathbf{J} \mathbf{W} \Sigma \mathbf{W}^T \mathbf{J}^T, \quad (7)$$

where Σ is the 3D covariance, derived from the scaling vector and rotation quaternion of this Gaussian [9], \mathbf{J} is the Jacobian of the camera projection described in Sec. III-A:

$$\mathbf{J} = \begin{bmatrix} \frac{\partial p_x}{\partial t_x} & \frac{\partial p_x}{\partial t_y} & \frac{\partial p_x}{\partial t_z} \\ \frac{\partial p_y}{\partial t_x} & \frac{\partial p_y}{\partial t_y} & \frac{\partial p_y}{\partial t_z} \\ 0 & 0 & 0 \end{bmatrix}, \quad (8)$$

with

$$\frac{\partial p_x}{\partial t_x} = +\frac{W}{2\pi} \cdot \frac{t_z}{t_x^2 + t_z^2}, \quad (9)$$

$$\frac{\partial p_x}{\partial t_y} = 0, \quad (10)$$

$$\frac{\partial p_x}{\partial t_z} = -\frac{W}{2\pi} \cdot \frac{t_x}{t_x^2 + t_z^2}, \quad (11)$$

$$\frac{\partial p_y}{\partial t_x} = -\frac{H}{\pi} \cdot \frac{t_x t_y}{t_r^2 \sqrt{t_x^2 + t_z^2}}, \quad (12)$$

$$\frac{\partial p_y}{\partial t_y} = +\frac{H}{\pi} \cdot \frac{\sqrt{t_x^2 + t_z^2}}{t_r^2}, \quad (13)$$

$$\frac{\partial p_y}{\partial t_z} = -\frac{H}{\pi} \cdot \frac{t_z t_y}{t_r^2 \sqrt{t_x^2 + t_z^2}}, \quad (14)$$

and \mathbf{W} is the rotation part of the 4×4 transformation matrix \mathbf{T}_{cw} from the world coordinate system to the camera space.

We also follow [10] in skipping the third row and column of $\tilde{\Sigma}$, in order to directly obtain the 2×2 covariance matrix. The forward process could be largely accelerated by the approximation Eq. (7), leading to high-FPS real-time rendering.

Overall, during the tile-based forward rendering process, a whole equirectangular image is partitioned into grids composed of tiles of the same size. First, the center and covariance of 3D Gaussians are projected onto the image screen. Second, each tile counts the 2D Gaussians whose radius of influence

covers this tile, generating one instance per influence. Third, all pixels within the same tile are rendered at the same time, each pixel assigned to one thread. These threads cooperatively get the attributes of the Gaussian instances observed by the current tile, then separately accumulate instances for α -blending until the pixel has $\alpha = 0.9999$. (The stopping threshold is not exactly 1 for numerical stability considerations.)

C. Backward Optimization

To optimize the world position \mathbf{m} , color c (derived from \mathbf{m} and Spherical Harmonics coefficients [9]), rotation \mathbf{q} , scale \mathbf{S} and opacity o of 3D Gaussians, we minimize the photometric loss between the rendered image I_r and ground truth I_{gt} :

$$\mathcal{L}(I_r, I_{gt}) = (1 - \lambda) |I_r - I_{gt}|_1 + \lambda(1 - \text{SSIM}(I_r, I_{gt})), \quad (15)$$

where $\text{SSIM}(I_r, I_{gt})$ is the structural similarity between two images, and λ is a balancing weight factor.

The backward gradient flows from \mathcal{L} to the attributes of 3D Gaussians through the full projection process. To be specific, except for c and o which have nothing to do with the camera model, the gradients of \mathcal{L} over the attributes are what we need to derive and modify for omnidirectional optimization. We can apply the chain rule for multivariable functions to obtain:

$$\frac{\partial \mathcal{L}}{\partial \mathbf{m}} = \sum_{k=1}^M \left[\frac{\partial \mathcal{L}}{\partial c} \frac{\partial c}{\partial \mathbf{m}} + \frac{\partial \mathcal{L}}{\partial \alpha_k} \frac{\partial \alpha_k}{\partial G_k} \left(\frac{\partial G_k}{\partial \tilde{\Sigma}} \frac{\partial \tilde{\Sigma}}{\partial \mathbf{J}} \frac{\partial \mathbf{J}}{\partial \mathbf{t}} \frac{\partial \mathbf{t}}{\partial \mathbf{m}} + \frac{\partial G_k}{\partial \mathbf{p}} \frac{\partial \mathbf{p}}{\partial \mathbf{s}} \frac{\partial \mathbf{s}}{\partial \mathbf{t}} \frac{\partial \mathbf{t}}{\partial \mathbf{m}} \right) \right], \quad (16)$$

$$\frac{\partial \mathcal{L}}{\partial \mathbf{q}} = \sum_{k=1}^M \left(\frac{\partial \mathcal{L}}{\partial \alpha_k} \frac{\partial \alpha_k}{\partial G_k} \frac{\partial G_k}{\partial \tilde{\Sigma}} \frac{\partial \tilde{\Sigma}}{\partial \Sigma} \frac{\partial \Sigma}{\partial \mathbf{R}} \frac{\partial \mathbf{R}}{\partial \mathbf{q}} \right), \quad (17)$$

$$\frac{\partial \mathcal{L}}{\partial \mathbf{S}} = \sum_{k=1}^M \left(\frac{\partial \mathcal{L}}{\partial \alpha_k} \frac{\partial \alpha_k}{\partial G_k} \frac{\partial G_k}{\partial \tilde{\Sigma}} \frac{\partial \tilde{\Sigma}}{\partial \Sigma} \frac{\partial \Sigma}{\partial \mathbf{S}} \right), \quad (18)$$

where M is the total number of instances generated by this Gaussian in all tiles, \mathbf{R} is the rotation matrix converted from quaternion \mathbf{q} . Vectors \mathbf{s} and \mathbf{p} are the screen-space and image-space coordinates, respectively. We retain the common portion from gradients given by [9], and replace the following parts

with our omnidirectional gradients: $\frac{\partial \tilde{\Sigma}}{\partial \Sigma}$, $\frac{\partial \mathbf{J}}{\partial \mathbf{t}}$, $\frac{\partial \mathbf{p}}{\partial \mathbf{s}}$, $\frac{\partial \mathbf{s}}{\partial \mathbf{t}}$.

IV. RECONSTRUCTION PIPELINE

The reconstruction of OmniGS starts from a set of SfM-calibrated equirectangular images $\{I_j\}$, each of which has a pose \mathbf{T}_j . We obtain initial 3D Gaussians \mathbb{G} from the sparse SfM point cloud \mathbb{P} , then begin a series of optimization iterations. For each iteration, we choose one view I_j from the randomly shuffled $\{I_j\}$, render from \mathbf{T}_j to get I_r , then compute $\mathcal{L}(I_r, I_j)$ and the corresponding backward gradients. After densifying \mathbb{G} based on the following strategies, we advance the optimizer by one step to optimize all 3D Gaussians.

We apply a gradient-based densification control strategy similar to [9]. But instead of using the perspective gradients, we judge whether to densify a Gaussian in sight of

Algorithm 1 Reconstruction Pipeline

Input: Equirectangular images $\{I_i\}$ with calibrated poses $\{\mathbf{T}_i\}$ and sparse SfM point cloud \mathbb{P}

Output: 3D Gaussians available for novel-view synthesis

Initialization : Create initial 3D Gaussians \mathbb{G} from \mathbb{P}

```

1: for  $j = 1$  to maximum iteration do
2:   pick a random  $i$ 
3:   render  $\mathbb{G}$  from  $\mathbf{T}_i$  to get  $I_r$ 
4:    $\mathcal{L}_j = \mathcal{L}(I_r, I_i) \leftarrow$  Eq. (15)
5:   backpropagate  $\mathcal{L}_j$ 
6:   if  $j \leq$  maximum densification iteration then
7:     if  $j \bmod$  densification interval  $== 0$  then
8:       densify  $\mathbb{G}$  by  $\frac{\partial \mathcal{L}_j}{\partial \mathbf{s}}$ 
9:       prune  $\mathbb{G}$  by  $o$ 
10:      prune  $\mathbb{G}$  by  $\mathbf{S}$ 
11:     end if
12:     if  $j \bmod$  opacity-resetting interval  $== 0$  then
13:       reset large  $o$  in  $\mathbb{G}$ 
14:     end if
15:   end if
16:   advance optimizer by one step
17: end for
18: return  $\mathbb{G}$ 

```

its gradient over omnidirectional screen-space location, i.e. $\frac{\partial \mathcal{L}}{\partial \mathbf{s}}$, which is derived and recorded during the calculation process in Sec. III-C. In detail, for Gaussians with a large enough gradient, if their scales are too large or too small, then they are going to be split or cloned respectively to densify \mathbb{G} , enhancing its ability to represent details. We also prune the Gaussians whose scale or screen-space radius is too large, intending to boost the details. Additionally, opacities of all Gaussians also contribute to the densification control. Gaussians with an excessively small opacity are pruned as well. Large opacities are reset to encourage more densification. We execute the densification control process periodically until reaching a certain number of iterations. We conclude the above reconstruction pipeline in Algorithm 1.

V. EVALUATION

We will report the evaluation results of OmniGS in this section. We compare our reconstruction quality and rendering speed with the baseline SOTA photorealistic 3D reconstruction methods, NeRF [8], Mip-NeRF 360 [20], 360Roam [5], Instant-NGP [21], TensoRF [22] and EgoNeRF [15]. We also conduct a cross-validation experiment to confirm the effectiveness of our method compared to the perspective 3DGS.

A. Implementation and Experiment Setup

We accomplish OmniGS based on the LibTorch framework, which is the C++ version of PyTorch. The tile-based omnidirectional rasterizer is implemented with custom CUDA kernels. As for the usage of datasets, we directly utilize the calibrated camera poses and sparse SfM point clouds

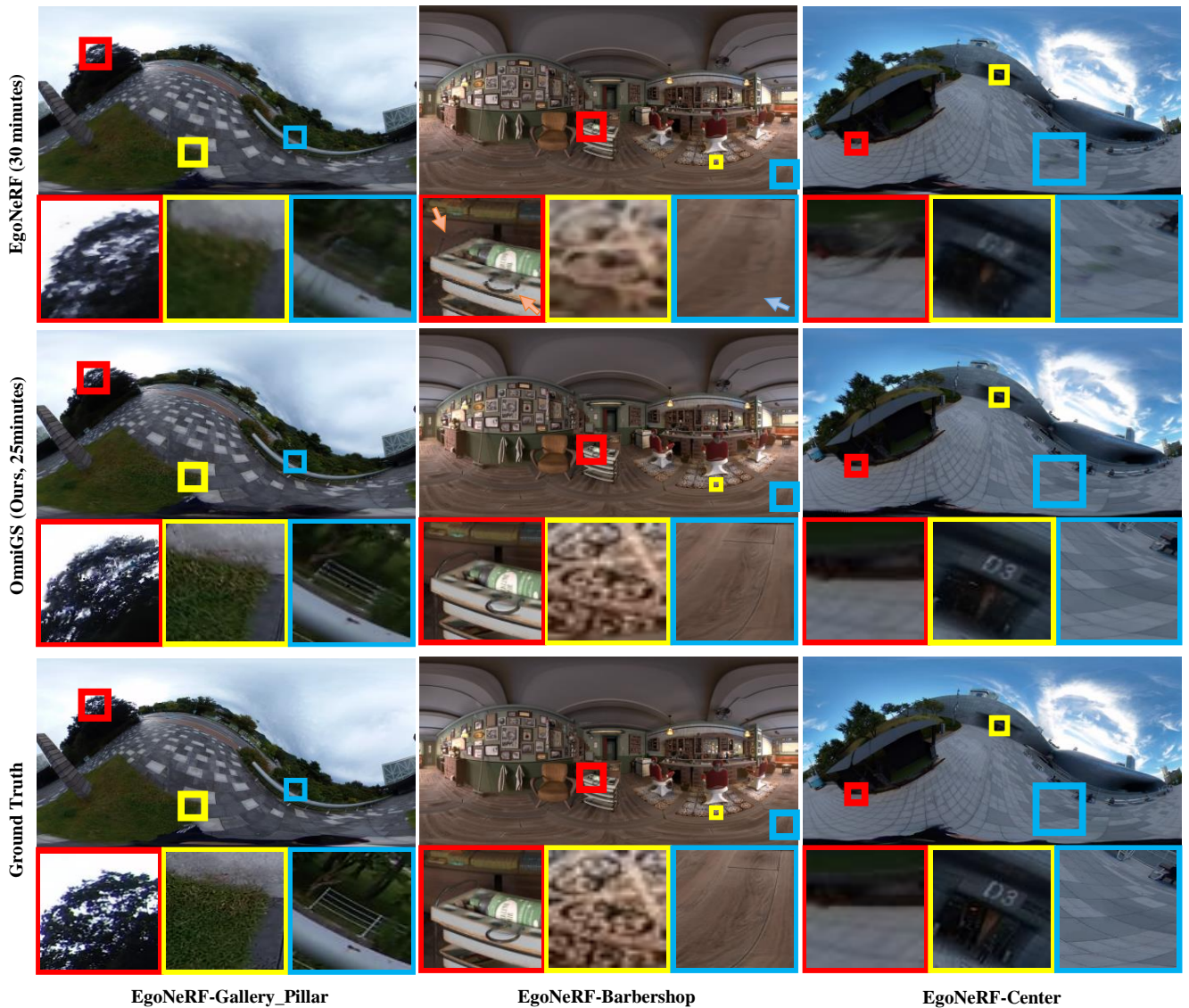


Fig. 3. Qualitative comparisons of omnidirectional novel-view synthesis in egocentric scenes. OmniGS can reconstruct the details more sharply and precisely with less training time, i.e., 25 mins.

contained in the datasets as initial input. But notably, we perform openMVG [16] SfM on the OmniBlender scenes of EgoNeRF dataset, since these scenes provide no sparse point clouds. Note that we skip the bottom part of the images when computing and backpropagating loss in 360Roam scenes since the base mobile robot is a dynamic object, which is beyond the scope of this paper. For the sake of a fair comparison, we use an RTX 3090 GPU to conduct all experiments on OmniGS, using the provided training and testing split, and gather the RTX-3090 baseline results reported by the authors of datasets [5] and [15] unless specifically stated. The resolutions actually used are also the original ones, i.e. 712×1520 for 360Roam, 1000×2000 for EgoNeRF-OmniBlender, and 960×1920 for EgoNeRF-Ricoh360. We evaluate the results in terms of PSNR, SSIM, LPIPS and rendering FPS, which are common

criteria for photorealistic reconstruction. The baselines, except for EgoNeRF, are evaluated in terms of perspective novel-view synthesis, regarding their original objective. We report the overall quantitative evaluation results in Table I.

B. Results and Evaluation

a) *On 360Roam dataset [5]:* 360Roam contains 11 complicated real-world indoor scenes. Our method gains a slightly higher performance above the SOTA Mip-NeRF 360, which uses a 1024-channel MLP network and needs several hours to train. We only takes less than 25 minutes to earn similar quality. Our rendering FPS is also about 100 times faster than Mip-NeRF 360, and at least four times higher than the other baselines. Note that EgoNeRF needs input images with an egocentric camera motion pattern, and therefore cannot be applied on 360Roam, in which the camera roams randomly

TABLE I
RECONSTRUCTION EVALUATION RESULTS.

Dataset	Method	PSNR \uparrow	SSIM \uparrow	LPIPS \downarrow	FPS \uparrow
360Roam	NeRF	22.443	0.672	0.339	<1
	Mip-NeRF 360	25.464	0.789	0.198	<1
	TensoRF	15.035	0.531	0.676	<1
	Instant-NGP	17.018	0.548	0.532	4
	360Roam	25.061	0.760	0.202	30
Ours	25.505	0.808	0.140	120	
Ego-O ^a	NeRF	25.095	0.711	0.446	<1
	Mip-NeRF 360	26.240	0.767	0.345	<1
	TensoRF	25.134	0.716	0.448	2
	EgoNeRF	29.326	0.858	0.177	2
	Ours	33.637	0.919	0.054	115
Ego-R ^b	NeRF	22.780	0.663	0.538	<1
	Mip-NeRF 360	24.280	0.725	0.384	<1
	TensoRF	23.820	0.694	0.481	2
	EgoNeRF	24.710	0.746	0.314	2
	Ours	26.034	0.825	0.131	93

^aEgoNeRF-OmniBlender. ^bEgoNeRF-Ricoh360.

TABLE II
QUALITATIVE COMPARISON OF PERSPECTIVE RENDERING RESULTS ON 360ROAM DATASET. P DENOTES PERSPECTIVE IMAGE, AND O DENOTES OMNIDIRECTIONAL IMAGE.

Method	Training	Rendering	PSNR \uparrow	SSIM \uparrow	LPIPS \downarrow
3DGS	P	O	22.698	0.755	0.243
		P	25.695	0.877	0.142
OmniGS (Ours)	O	O	25.505	0.808	0.140
		P	27.505	0.889	0.097

in the scenes. In addition, 360-GS [19] reports an FPS of 60 in indoor scenes with a resolution of 512×1024 , which is slower than ours due to its two-stage projection. It also fails to deal with the multiple-room scenes of 360Roam because of its dependence on single-room layout prediction networks.

b) *On EgoNeRF dataset [15]*: EgoNeRF provides 11 OmniBlender simulation scenes and 12 Ricoh360 real-world scenes. We train OmniGS to 32k iterations on them, taking around 25 minutes per scene. We gather the results of 10k iterations for the baselines, since EgoNeRF takes around 30 minutes to finish them. Quantitative evaluation results demonstrate that our OmniGS outperforms the SOTA EgoNeRF in terms of both quality and rendering speed (PSNR+4.311, SSIM+0.061, LPIPS-0.123, FPS 57.5 times on OmniBlender, and PSNR+1.324, SSIM+0.079, LPIPS-0.183, FPS 46.5 times on Ricoh360). We also spend less time on training to acquire such performance. Fig. 3 shows some qualitative comparison examples of omnidirectional rendering, illustrating the ability of OmniGS to reconstruct clearer and sharper details.

C. Additional Evaluation in Perspective Rendering

With a view to validate the effectiveness of our method, we use openMVG to divide each equirectangular image into 6 perspective images and train the 360Roam scenes again with the perspective 3DGS [9]. We run the optimization process to the same densification time and total time. Perspectives including the base mobile robot are skipped, for the same reason stated in Sec. V-A. We re-evaluate the OmniGS results by cropping the rendered testing views into perspective images.

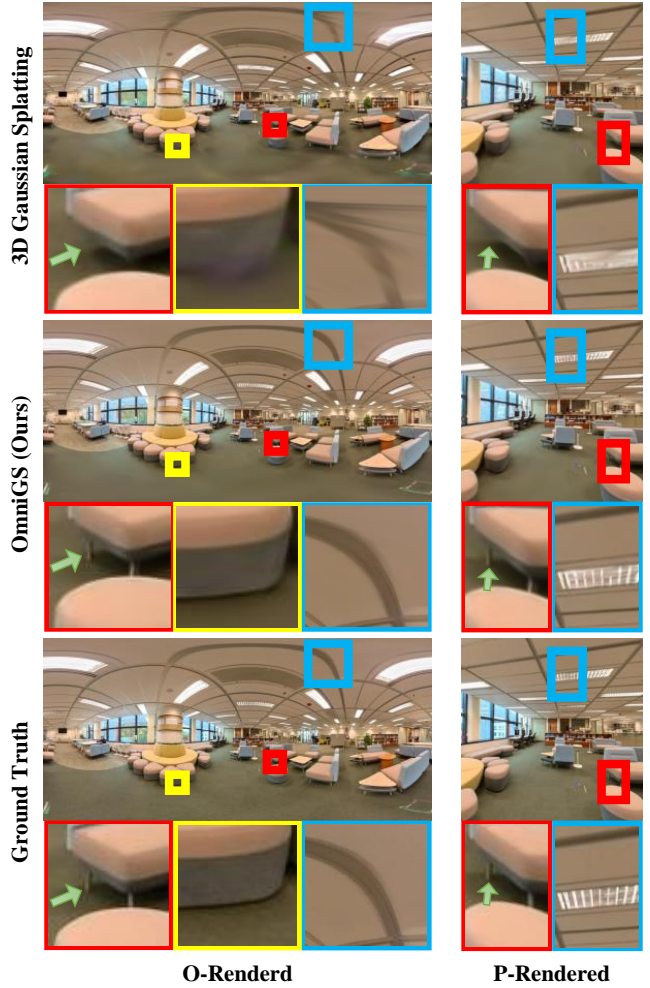


Fig. 4. Example results of the evaluation in perspective rendering. P denotes perspective image, and O denotes omnidirectional image. The perspective 3DGS suffers detail loss and artifacts caused by the limited FoV utilization rate, while OmniGS renders correct omnidirectional novel views that can be cropped to better perspective images.

As shown in Table II, quantitative results indicate that our method is equipped with the ability to generate better perspective views cropped from the rendered omnidirectional images (PSNR+1.81, SSIM+0.012, LPIPS-0.045). In addition, we render the 3DGS-trained models with our omnidirectional rasterizer. The omnidirectional novel-view synthesis quality of our models is also higher than that of 3DGS (PSNR+2.807, SSIM+0.053, LPIPS-0.103). Moreover, qualitative results (Fig. 4) figure out that the perspective 3DGS tends to lose detail and suffer artifacts due to the low utilization rate of observations. It can use only one limited view at one time. In contrast, OmniGS makes use of the whole omnidirectional environment in each iteration, reaching more robust densification and faster model convergence. At the same time, the omnidirectional images rendered from OmniGS-reconstructed models can be cropped to perspective views properly, showing the strong scalability of our method.

VI. CONCLUSION AND DISCUSSION

In this paper, we present a novel fast photorealistic 3D reconstruction method, named OmniGS, which fully exploits the speed advantage of direct omnidirectional screen-space splatting. We derived the backward gradient and implemented a real-time tile-based omnidirectional rasterizer. Experiment results on various datasets show that OmniGS achieves SOTA reconstruction quality and rendering FPS, even with less training time. The evaluation in perspective rendering indicates that by cropping the rendered omnidirectional images into perspective ones, our method can generate better perspective views than the original 3DGS.

We believe OmniGS holds the potential to evolve in various directions. Firstly, considering the approximation nature of screen-space splatting, we ignore impacts due to the periodicity of trigonometric functions, to pursue higher speed. Better quality may be realized by taking it into account and sacrificing more computational resources. Secondly, OmniGS could join with omnidirectional SLAM schemes to form real-time simultaneous localization and photorealistic mapping systems similar to perspective ones [14], leading to more robotics applications.

REFERENCES

- [1] K. Y. Y. L. D. W. San Jiang and C. Wu, "3D reconstruction of spherical images: a review of techniques, applications, and prospects," *Geo-spatial Information Science*, pp. 1–30, 2024.
- [2] H. Huang and S.-K. Yeung, "360VO: Visual odometry using a single 360 camera," in *International Conference on Robotics and Automation (ICRA)*. IEEE, 2022.
- [3] Q. Wu, X. Xu, X. Chen, L. Pei, C. Long, J. Deng, G. Liu, S. Yang, S. Wen, and W. Yu, "360-VIO: A robust visual-inertial odometry using a 360° camera," *IEEE Transactions on Industrial Electronics*, pp. 1–10, 2023.
- [4] Z. Wang, K. Yang, H. Shi, P. Li, F. Gao, J. Bai, and K. Wang, "LF-VISLAM: A SLAM framework for large field-of-view cameras with negative imaging plane on mobile agents," *IEEE Transactions on Automation Science and Engineering*, pp. 1–15, 2023.
- [5] H. Huajian, C. Yingshu, Z. Tianjia, and Y. Sai-Kit, "360Roam: Real-time indoor roaming using geometry-aware 360° radiance fields," *arXiv preprint, arXiv:2208.02705*, 2022.
- [6] S. Kulkarni, P. Yin, and S. Scherer, "360FusionNeRF: Panoramic neural radiance fields with joint guidance," in *2023 IEEE/RSJ International Conference on Intelligent Robots and Systems (IROS)*, 2023, pp. 7202–7209.
- [7] Z. Chen, Y.-P. Cao, Y.-C. Guo, C. Wang, Y. Shan, and S.-H. Zhang, "PanoGRF: Generalizable spherical radiance fields for wide-baseline panoramas," in *Thirty-seventh Conference on Neural Information Processing Systems*, 2023.
- [8] B. Mildenhall, P. P. Srinivasan, M. Tancik, J. T. Barron, R. Ramamoorthi, and R. Ng, "NeRF: Representing scenes as neural radiance fields for view synthesis," in *European Conference on Computer Vision (ECCV)*, 2020.
- [9] B. Kerbl, G. Kopanas, T. Leimkuehler, and G. Drettakis, "3D gaussian splatting for real-time radiance field rendering," *ACM Transactions on Graphics*, vol. 42, no. 4, 2023.
- [10] M. Zwicker, H. Pfister, J. van Baar, and M. Gross, "EWA splatting," *IEEE Transactions on Visualization and Computer Graphics*, vol. 8, no. 3, pp. 223–238, 2002.
- [11] N. Keetha, J. Karhade, K. M. Jatavallabhula, G. Yang, S. Scherer, D. Ramanan, and J. Luiten, "SplatTAM: Splat, track & map 3D gaussians for dense RGB-D SLAM," *arXiv preprint, arXiv:2312.02126*, 2023.
- [12] C. Yan, D. Qu, D. Wang, D. Xu, Z. Wang, B. Zhao, and X. Li, "GS-SLAM: Dense visual SLAM with 3D gaussian splatting," *arXiv preprint, arXiv:2311.11700*, 2024.
- [13] V. Yugay, Y. Li, T. Gevers, and M. R. Oswald, "Gaussian-SLAM: Photo-realistic dense SLAM with gaussian splatting," *arXiv preprint, arXiv:2312.10070*, 2023.
- [14] H. Huang, L. Li, H. Cheng, and S.-K. Yeung, "Photo-SLAM: Real-time simultaneous localization and photorealistic mapping for monocular, stereo, and RGB-D cameras," in *Proceedings of the IEEE/CVF Conference on Computer Vision and Pattern Recognition (CVPR)*, in press, 2024.
- [15] C. Choi, S. M. Kim, and Y. M. Kim, "Balanced spherical grid for egocentric view synthesis," in *Proceedings of the IEEE/CVF Conference on Computer Vision and Pattern Recognition (CVPR)*, 2023, pp. 16 590–16 599.
- [16] P. Moulon, P. Monasse, R. Perrot, and R. Marlet, "OpenMVG: Open multiple view geometry," in *Reproducible Research in Pattern Recognition*, 2017, pp. 60–74.
- [17] G. Wang, P. Wang, Z. Chen, W. Wang, C. C. Loy, and Z. Liu, "PERF: Panoramic neural radiance field from a single panorama," *Technical Report*, 2023.
- [18] H. Matsuki, R. Murai, P. H. J. Kelly, and A. J. Davison, "Gaussian Splatting SLAM," in *Proceedings of the IEEE/CVF Conference on Computer Vision and Pattern Recognition (CVPR)*, in press, 2024.
- [19] J. Bai, L. Huang, J. Guo, W. Gong, Y. Li, and Y. Guo, "360-GS: Layout-guided panoramic gaussian splatting for indoor roaming," *arXiv preprint, arXiv:2402.00763*, 2024.
- [20] J. T. Barron, B. Mildenhall, D. Verbin, P. P. Srinivasan, and P. Hedman, "Mip-NeRF 360: Unbounded anti-aliased neural radiance fields," in *Proceedings of the IEEE/CVF Conference on Computer Vision and Pattern Recognition (CVPR)*, 2022, pp. 5470–5479.
- [21] T. Müller, A. Evans, C. Schied, and A. Keller, "Instant neural graphics primitives with a multiresolution hash encoding," *ACM Transactions on Graphics*, vol. 41, no. 4, 2022.
- [22] A. Chen, Z. Xu, A. Geiger, J. Yu, and H. Su, "TensorRF: Tensorial radiance fields," in *European Conference on Computer Vision (ECCV)*, 2022, pp. 333–350.